Invited Article: Label-free nerve imaging with a coherent anti-Stokes Raman scattering rigid endoscope using two optical fibers for laser delivery

Keigo Hirose, Shuichiro Fukushima, Taichi Furukawa, Hirohiko Niioka, and Mamoru Hashimoto

Citation: APL Photonics **3**, 092407 (2018); doi: 10.1063/1.5031817
View online: https://doi.org/10.1063/1.5031817
View Table of Contents: http://aip.scitation.org/toc/app/3/9
Published by the American Institute of Physics

Invited Article: Label-free nerve imaging with a coherent anti-Stokes Raman scattering rigid endoscope using two optical fibers for laser delivery

Keigo Hirose,[1] Shuichiro Fukushima,[1] Taichi Furukawa,[2] Hirohiko Niioka,[3] and Mamoru Hashimoto[4,a]
[1]*Graduate School of Engineering Science, Osaka University, Osaka, Japan*
[2]*Faculty of Engineering, Yokohama National University, Yokohama, Japan*
[3]*Institute for Datability Science, Osaka University, Osaka, Japan*
[4]*Graduate School of Information Science and Technology, Hokkaido University, Hokkaido, Japan*

(Received 31 March 2018; accepted 26 June 2018; published online 27 July 2018)

A coherent anti-Stokes Raman scattering (CARS) rigid endoscope using two optical fibers to deliver excitation beams individually is developed. The use of two optical fibers allows the correction of longitudinal chromatic aberration and enhances the CARS signal by a factor of 2.59. The endoscope is used to image rat sciatic nerves with an imaging time of 10 s. Imaging of the rabbit prostatic fascia without sample slicing is also demonstrated, which reveals the potential for the application of the CARS endoscope to robot-assisted surgery. https://doi.org/10.1063/1.5031817

I. INTRODUCTION

Robot-assisted surgery most commonly involves the performance of endoscopic surgical procedures under guidance by a robotic system.[1–3] For example, surgeons are able to observe and identify lesions using a rigid endoscope and then operate upon these using interactive robotic arms equipped with the appropriate tools and passing through small incisions. Because of the reductions in blood loss and pain that can be achieved with the use of high-precision robot-assisted surgery, this is less physically taxing for the patient and allows more rapid recovery compared with conventional open surgery.

To preserve patients' neurological functions, it is important to retain nerves as much as possible during surgery and nerve-sparing procedures have been introduced into robot-assisted surgery.[4,5] For such procedures to be successful, identification of nerves is required during surgery. Rigid endoscopes provide high-resolution, high-magnification, and three-dimensional images,[6] but it is still necessary for surgeons to determine the segments to be excised by observing subtle absorption differences under visible light and utilizing their anatomical knowledge. Therefore, effective imaging of nerves will improve the procedural success rate.

Label-free visualization of nerves using Raman microscopy has been proposed and demonstrated.[7,8] Raman scattering provides information about molecular vibrations, which are sensitive to the molecular species involved, and thus a map of molecular species can be obtained. By using the higher Raman shift region around 2900 cm^{-1}, mapping of both myelinated and unmyelinated nerves, fibrous connective tissues, and adipose tissues of the human prostate has been demonstrated by using spontaneous Raman scattering. One disadvantage of spontaneous Raman microscopy is the long measurement time that is required owing to the low cross sections for Raman scattering, and parallel excitation/detection methods have been proposed to reduce imaging times.[9]

[a]hashimoto@ist.hokudai.ac.jp

Another method to improve imaging times is the use of nonlinear coherent Raman scattering.[10,11] Nonlinear coherent Raman microscopy using ultrafast lasers allows video-rate or faster Raman imaging.[12–15] Nerve imaging by nonlinear coherent Raman microscopy and its medical applications have been vigorously studied.[16–21] Nonlinear coherent Raman imaging has another feature of high-definition imaging compared with spontaneous Raman imaging. Spontaneous Raman scattering provides a Raman spectrum of each pixel in the image; however, low intensity of Raman scattering limits the pixel size of imaging. High intensity of nonlinear coherent Raman scattering provides high-definition imaging, which is useful in surgical procedures to identify the excision site. The present authors have developed a rigid endoscope based on coherent anti-Stokes Raman scattering (CARS, which is one type of nonlinear Raman scattering) and have demonstrated its use in nerve imaging.[22]

In this paper, we describe a modification of the CARS rigid endoscope using two optical fibers for separate delivery of the imaging laser beams, thereby correcting longitudinal chromatic aberration, and we demonstrate its application to nerve imaging of rat sciatic nerves and rabbit periprostatic nerves.

II. MATERIALS AND EXPERIMENTAL SETUP

A. Sample preparation

1. Rat sciatic nerve

A formalin-fixed sciatic nerve of a Sprague Dawley rat was purchased from the Japan Lamb Co., Ltd., and was used as a sample. It was cut along the axis to observe the nerve fibers and then sandwiched between a coverslip and a slide glass using a silicone spacer (2 mm thickness), with the gap being filled with phosphate-buffered saline to prevent drying.

2. Rabbit periprostatic nerve

We prepared two types of samples of rabbit periprostatic nerves: one type was sliced, while the others were tissues without slicing. Formalin-fixed rabbit urinary organs including a prostate were purchased from the Japan Lamb Co., Ltd. (Fig. 1). The first type of samples was 10 μm-thick serial sections of the periprostatic tissue sliced parallel to the urethra on the dorsal side, perpendicular to the image shown in Figs. 1(b) and 1(c), to show the fibrous structure of nerves. Half of the adjacent slices were stained with Luxol Fast Blue (LFB) to visualize nerves, and the others without staining were used for CARS endoscopic observations. The samples without slicing were divided into two groups. For fluorescence imaging using two-photon excitation, multilayered tissue was cut from the prostatic fascia and doubly stained with FluoroMyelin Green and DAPI (4′,6-diamidino-2-phenylindole) for visualizing lipids and the nucleus, respectively. For CARS imaging using the endoscope that we have developed, a layer of the prostatic fascia was peeled off to simultaneously observe the transmittance image for finding the nerves. The typical thickness of a layer of the prostatic fascia was 100 μm.

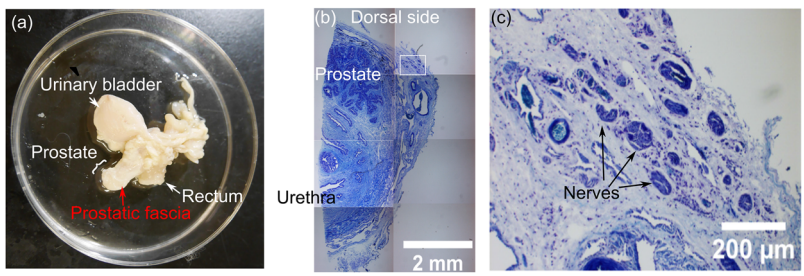

FIG. 1. (a) Photograph of rabbit urinary organs. (b) Cross section image of the prostate stained with Luxol Fast Blue. (c) Expanded image of the white box in (b).

B. Development of a rigid coherent anti-Stokes Raman scattering endoscope using two optical fibers

The system is similar to that previously reported,[22] but the method of laser beam delivery is different. In the previous system, two laser beams were superimposed and delivered via a single-mode fiber. In the present system, two laser beams are delivered individually via two polarization-maintained single-mode fibers and are superimposed in the endoscope head to allow adjustment for the chromatic aberration of the lenses. The following is a brief description of the system.

The system, as shown schematically in Fig. 2(a), employs as light sources two synchronized pulsed lasers with different wavelengths (ω_1 and ω_2), two polarization-maintaining fibers, and a rigid endoscope head, a photograph of which is shown in Fig. 2(b).

The lasers are both picosecond mode-locked Ti:sapphire lasers. The ω_1 laser (Tsunami, Spectra-Physics) has a pulse duration of 5 ps and a repetition rate of 80 MHz. The ω_2 laser (ps-AOTF, Megaopt) has a pulse duration of <20 ps and a repetition rate of 80 MHz and is mounted with an acoustically tunable optical filter (AOTF) modified to allow synchronization with the ω_1 laser.[13] Even though the wavelength of the ω_2 laser is electrically tunable, the wavelengths of the ω_1 and ω_2 laser beams are fixed at 709 and 888 nm, respectively, to visualize lipids of nerves included in myelin sheaths using CH_2 symmetric stretching at a Raman shift of 2845 cm^{-1}. The two laser pulses are temporally synchronized with a synchronization system,[23] and the temporal time difference between two pulses is adjusted with an optical delay stage (Delay).

Each beam is coupled into a polarization-maintaining single-mode fiber (PMF: P1-630PM-FC-2 for the ω_1 laser beam and P1-780PM-FC-2 for the ω_2 laser beam, Thorlabs; 2 m) with a fiber coupler (FC: PAFA-X-4-B, Thorlabs). Each individual beam is coupled out with a fiber collimator (FC: RC04FC-P01 for the ω_1 beam and ZC618-B for the ω_2 beam, Thorlabs) and superimposed on a short-wavelength-path filter (SF: FES0800, Thorlabs).

The overlapped beams are reflected by a pair of galvano mirrors (GS: GVS002, Thorlabs) for scanning the beams to observe *XY* images, relayed with a pair of lenses (RL: TS achromatic lens 9 × 75 VIS-NIR INK, Edmund; f = 75 mm) in a tube with a diameter of 12 mm and a length of 270 mm, and are focused with an achromatic objective lens (OL1: AC050-008-B-ML, Thorlabs; f = 7.5 mm, lens diameter 5.0 mm, working distance 4.2 mm). The backscattered CARS emission is reflected by a dichroic mirror (DM: FF660-Di02-25 × 36, Semrock), separated from the excitation beams through five optical filters (F: FF01-609/54-25, FF01-591/6-25, FF01-680/SP-25, Semrock; 3rd560-640, Omega; FESH0650, Thorlabs), and then detected with a photomultiplier tube (PMT: C9110, Hamamatsu). The sample is placed on a *Z*-axis stepping motor stage (STG: OSMS80-20ZF, Sigmakoki), and the transmitted excitation light is detected with a silicon photodiode (PD) through an objective (OL2) to allow simultaneous observation of the transmission image. Since we use PMFs,

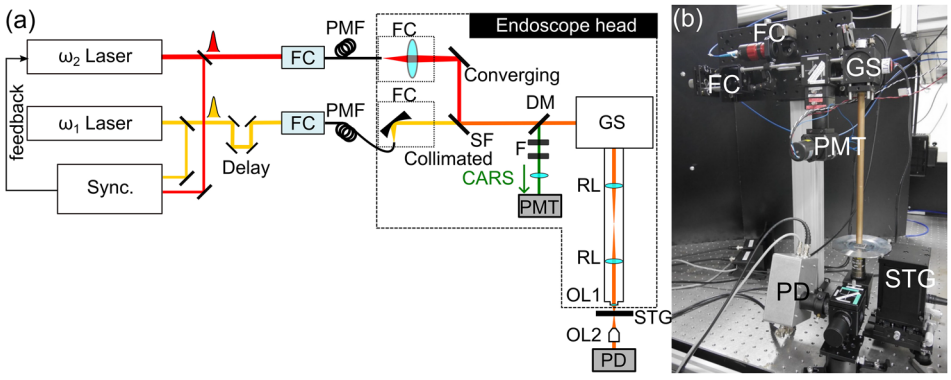

FIG. 2. (a) Schematic diagram of the coherent anti-Stokes Raman scattering endoscopy system. Sync.: synchronization controller; FC: fiber coupler; PMT: photomultiplier tube; PMF: polarization-maintaining single-mode fiber; SF: short wavelength pass filter; DM: dichroic mirror; F: optical filter; GS: galvano mirrors; RL: relay lens; OL: objective lens; STG: mechanical stage; PD: photodiode. (b) Photograph of the endoscope head.

both beams are linear polarization. The direction of polarization of both beams was fixed to the horizontal direction in figures.

1. Estimation of longitudinal chromatic aberration

The longitudinal (i.e., along the optical axis) chromatic aberration of the system was estimated by observing the longitudinal distance between the focal spots of the two beams. A GaAsP photodiode (G1115, Hamamatsu) placed on the stepping motor stage (STG) and a current amplifier (PDA200C, Thorlabs) were used to determine the focal spots. Since the photodiode has a wide bandgap (<680 nm in wavelength), it only responds to two-photon absorption for the ω_1 (709 nm) and ω_2 (888 nm) laser beams.[24] The position of the photodiode is scanned along the optical axis, and the response to two-photon absorption, represented by the square of the laser intensity, is the largest at the focal spot.

C. Two-photon fluorescence imaging

Fluorescence images were observed with a two-photon excited fluorescence microscope (MPM200-2, Thorlabs). As the light source, a femtosecond Ti:sapphire laser (Femto Source Pro, Femto Laser) with a pulse duration of 12 fs and a repetition rate of 80 MHz was used, and chirps in the optics were corrected with a pulse compressor (FSPC, Thorlabs). Resonant galvano mirrors were incorporated in the microscope and two-photon fluorescence images were observed at 15.0 frames/s. A water-immersion objective lens (N20X-PFH, Olympus; ×20, NA = 1.0) was used for imaging. The number of imaging pixels was 1024×1024, and the imaging area was $810 \times 810\ \mu m^2$. In the fluorescence images, signals from FluoroMyelin Green and DAPI are shown as green and blue, respectively.

III. RESULTS AND DISCUSSION

We previously reported that CARS endoscopy using a single-mode optical fiber for delivering the beams suffered from large longitudinal chromatic aberration, even though the relay lenses and the objective lens were achromatic. Chromatic aberration reduces spatial resolution and causes color fringing in conventional imaging systems, while it reduces the signal in CARS imaging systems because CARS is sensitive to overlapping of two excitation beams.

In the present system, the two excitation beams are delivered individually via two single-mode optical fibers, with one of the beams (the ω_1 beam) being coupled out with a zooming fiber coupler. As a result, the longitudinal focal position of the ω_1 beam can be adjusted.

It can be seen from Fig. 3(a) that the previous system exhibits a 21 μm focal shift between the two laser beams, but, as can be seen in Fig. 3(b), chromatic aberration is corrected in the present system. This correction of longitudinal chromatic aberration enhances the CARS signals. Figures 3(c) and 3(d) show the results of CARS imaging of polystyrene beads (diameter 10 μm) in water using the previous and present systems, respectively. The background subtracted CARS intensity of four polystyrene beads shown in inset of Fig. 3(d) is 2.59 times higher than that in that of Fig. 3(c). However, the mean and standard deviation of the background are also 2.46 and 1.58 times increased, respectively. As a result, when the standard deviation of the background is defined as noise, the signal to noise ratio is 1.62 times improved. Figure 3(e) (Multimedia view) shows the imaging results for a rat sciatic nerve observed with five accumulations of 2 s/image. These images were obtained by scanning the sample along the optical axis in 2 μm steps. The fibrous structure of the sciatic nerve can clearly be seen.

We observed rabbit periprostatic nerves to visualize nerves in tissue. To compare the CARS image with the stained image at the adjacent regions, we prepared a serial section of the prostate tissue, one of which was unstained and the other was stained. Figure 4 shows imaging results of the rabbit prostate stained with LFB (a), together with transmission (b) and CARS (c) images without staining. LFB stains myelin sheath blue, and so the dark blue regions with cord-like structure shown in Fig. 4(a) are identified as nerves. Similar structures are seen in the CARS image in Fig. 4(c). Figure 4(d) is a line profile of CARS intensity along the white box in (c). The profile is averaged by 15 pixels in the

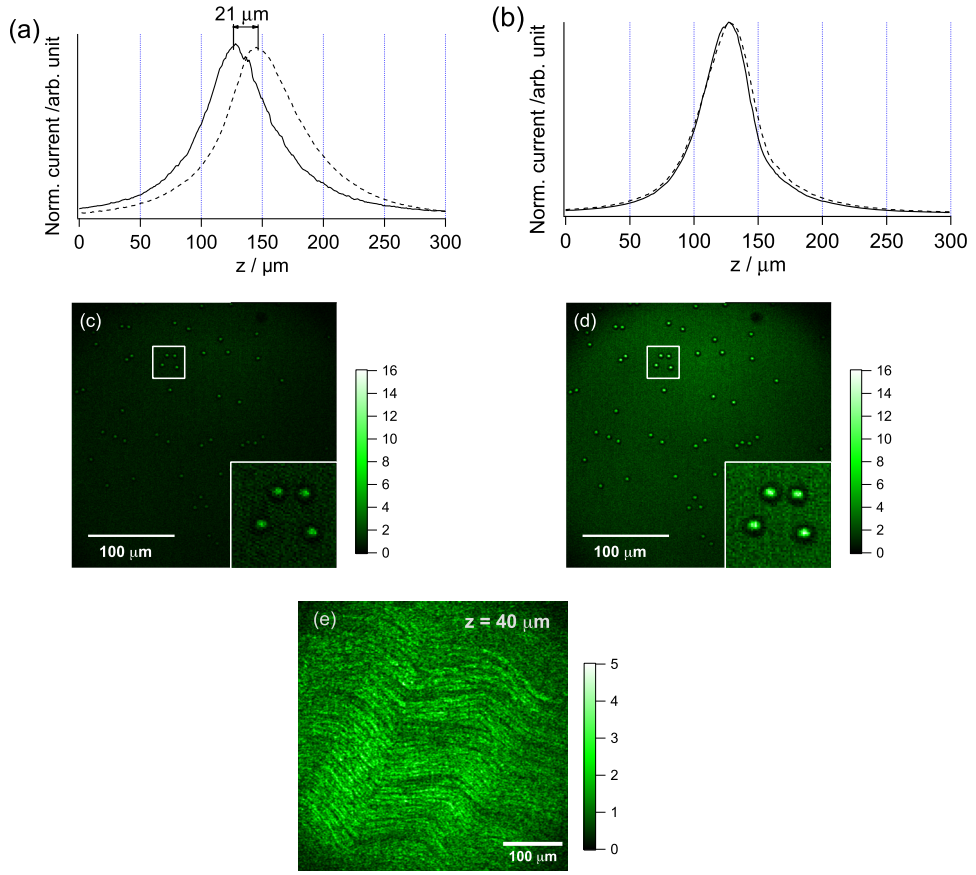

FIG. 3. [(a) and (b)] Correction of longitudinal chromatic aberration: longitudinal focal positions of ω_1 (solid line) and ω_2 (dashed line) observed (a) with the previous system using a single-mode fiber and (b) with the present system using two single-mode fibers. [(c) and (d)] Comparison of CARS intensity of polystyrene beads observed with (c) the previous and (d) the present systems. The inset at the bottom right on each figure is an expanded image of the white box. The images are 500 × 500 pixels, the powers of the laser beams were 30 mW (ω_1) and 15 mW (ω_2) at the sample, and the images were observed with 10 accumulations of 2 s/image. (e) CARS imaging of a rat sciatic nerve observed with 10 s/image. The images are 500 × 500 pixels, the powers of the laser beams were 100 mW (ω_1) and 50 mW (ω_2) at the sample, and the images were observed with five accumulations of 2 s/image. Multimedia view: https://doi.org/10.1063/1.5031817.1

horizontal. Since a large background that reaches 2/3 of the peak signal is superimposed, the image contrast is not so high.

To simulate surgery, we also observed the rabbit prostatic fascia without slicing. Figure 5(a) shows an image of the rabbit prostatic fascia observed with a two-photon fluorescence microscope, while Figs. 5(b) and 5(c) show a transmittance image and a CARS image, respectively, both observed

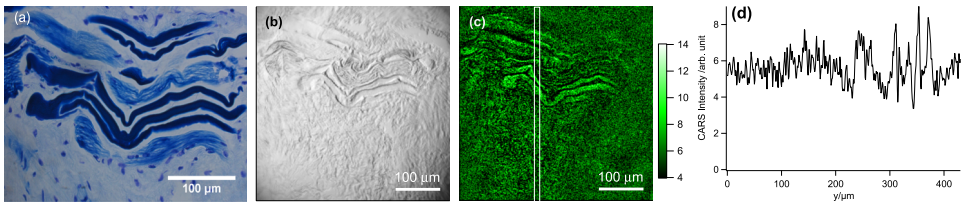

FIG. 4. (a) LFB-stained image of a 10 μm-thick section. (b) Transmittance and (c) CARS images of the serial section in (a) without staining. (d) Line profile of CARS intensity at the white box shown in (c). The laser powers at the sample to observe (b) and (c) were 30 mW (ω_1) and 12 mW (ω_2). The number of pixels is 500 × 500, and there were 100 accumulations with 4 s/image.

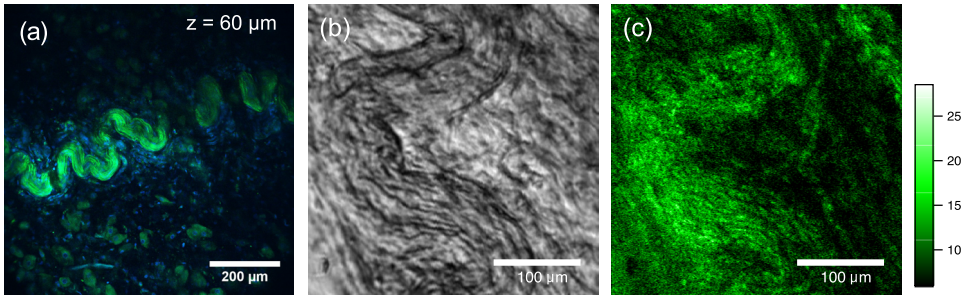

FIG. 5. (a) Two-photon fluorescence image of prostatic fascia. [(b) and (c)] Images of prostatic fascia obtained using the CARS endoscope: (b) transmittance image; (c) CARS image. For CARS imaging, the powers of the laser beams were 100 mW (ω_1) and 50 mW (ω_2) at the sample, and there were 100 accumulations with 2 s/image. The number of pixels is 500×500.

with the CARS endoscope. The fluorescence image shows (in green) a winding fibrous structure at $Z = 60$ μm from the sample surface. In both Figs. 5(b) and 5(c), a winding fibrous structure similar to that in Fig. 5(a) can clearly be seen. The structures in these images from the CARS endoscope can thus be identified as nerves.

We have thus succeeded in nerve imaging with 10 s total exposure time. However, a long exposure time was required for imaging of periprostatic nerves compared with the sciatic nerve. Much faster imaging is required for surgery because the surgeon cannot wait for so long during an operation.

The fact that a very thin sample was used is a possible reason for the long exposure time needed for CARS imaging. Since CARS emission is radiated mainly in the forward direction, it penetrates easily through a thin specimen and its intensity becomes low.[12] The thickness of sliced samples was 10 μm and that of the prostate fascia was about 100 μm. The use of a thicker sample should provide larger CARS signals as a result of multiple scattering in the sample. According to the literature,[12] intensity of the backscatterd CARS from the tissue (thicker than 200 μm) increases about 30 times comparing with 10 μm thickness samples. Although the thickness of the prostate fascia was about 100 μm, its transmittance was 89%. The 89% transmittance corresponds to 7.8 μm thickness with a scattering of coefficient 150 cm^{-1} which is the typical scattering coefficient of tissues.[12] Anyway, since the generated forward CARS radiation transmits the sample, epi-detected signal is reduced. Therefore, second-order imaging, about 30 times faster imaging, is expectable for thick tissue imaging.

The NA (numerical aperture) of the objective lens is 0.26 because the effective diameter and the focal length of the objective are 4 mm and 7.5 mm, respectively. However, the diameter of the laser beams (~2.0 mm) substantially limits the effective NA of the endoscopy system to only 0.13. Increasing the NA should be possible to improve the CARS intensity and imaging speed. One way to increase the effective NA is to increase the diameter of the beam, and the other is to use an objective lens with a short focal length. Increasing of the beam diameter will be easily applicable without any side effects. Using a short focus-length objective will reduce the view area and working distance. A relay lens system using shorter focal-length lenses is required to keep the view area. Because of high scattering of the tissue, the penetration depth of the excitation beams might be limited to several hundred micrometers. Therefore, when the working distance of the objective is larger than several millimeters, the short working distance might not be so severe for imaging. Rather, contamination by blood becomes a problem and it may be necessary to provide a cleaning system of the objective.

High-definition imaging is a feature of nonlinear coherent Raman imaging. Since we target myelinated nerves by observing CH_2 stretching of lipids, the adipose tissue also provides a large signal. However, the morphology of lipid droplets is completely different than that of nerves. High-definition imaging of nonlinear coherent Raman scattering clearly shows the morphology of nerves and adipose tissues and enables the identification of nerves.

The non-resonant background also reduces the imaging contrast and the quantitativity of lipids; however, the morphological information supports the discrimination of nerves. The background shown in Fig. 4 might be the effect of the non-resonant background and CH_2 group contained in

non-neuronal tissues. Even though the high background reduces the contrast of CARS imaging, clear intensity difference is obtained. Transmission and CARS images provide information about the structure, but the CARS image is able to give information about the intensity and morphology of the structure. Therefore, endoscopic CARS imaging has high potential for nerve identification.

Unmyelinated nerves of autonomic nerves also play an important role in autonomic functions. The identification of unmyelinated nerves was studied using spontaneous Raman microscopy, and unmyelinated nerves were separable from the other tissues only using high Raman shift region signals around 2900 cm^{-1}. In this case, the CARS spectral imaging and spectral analysis will also be required to identify the unmyelinated nerves.

In the present system, we manually adjust the focal position to correct the longitudinal chromatic aberration. Electrical control of the focal position will be useful for spectral imaging of CARS endoscopy. The focal position depends on the wavelength of the excitation beam, and to observe a wide Raman shift range, wavelength tuning of the excitation beam is required. Thus, adjusting the focal position together with wavelength tuning will improve the observable Raman shift range, particularly with the use of a higher numerical aperture, which would reduce the size of the focal volume and sensitivity to the longitudinal chromatic aberration.

Observation of the CARS endoscope will be performed after the hemostasis, blood washing, and suction. However, the influence of the remaining blood is a problem and more studies are required for clinical use.

IV. CONCLUSION

We have developed a CARS endoscopy system with the correction of longitudinal chromatic aberration using two optical fibers for laser delivery. By adjusting the focal position of one of the excitation beams, the intensity of CARS is improved by a factor of 2.59. We have demonstrated imaging of nerves with 10 s imaging time using this endoscope. CARS imaging of a serial section of the rabbit periprostatic tissue has been compared with imaging of a stained section, and CARS imaging of the rabbit prostatic fascia without slicing has also been demonstrated. Since CARS imaging of nerves provides information on both the morphology and intensity of structures that are observed, it should allow improved visualization of nerves during surgery.

ACKNOWLEDGMENTS

This work was supported in part by the Japan Agency for Medical Research and Development (AMED) under Collaborative Research Based on Industrial Demand "*In Vivo* Molecular Imaging: Towards Biophotonics Innovations in Medicine" (No. 15im0402007h0005) and the Japan Society for the Promotion of Science (JSPS) Grant-in-Aid for Scientific Research B (No. 17H0279307).

[1] A. Tewari, A. Srivastava, and M. Menon, BJU Int. **92**, 205 (2003).
[2] Q.-D. Trinh, J. Sammon, M. Sun, P. Ravi, K. R. Ghani, M. Bianchi, W. Jeong, S. F. Shariat, J. Hansen, J. Schmitges, C. Jeldres, C. G. Rogers, J. O. Peabody, F. Montorsi, M. Menon, and P. I. Karakiewicz, Eur. Urol. **61**, 679 (2012).
[3] B. H. Bochner, G. Dalbagni, D. D. Sjoberg, J. Silberstein, G. E. K. Paz, S. M. Donat, J. A. Coleman, S. Mathew, A. Vickers, G. C. Schnorr, M. A. Feuerstein, B. Rapkin, R. O. Parra, H. W. Herr, and V. P. Laudone, Eur. Urol. **67**, 1042 (2015).
[4] M. Menon, S. Kaul, A. Bhandari, A. Shrivastava, A. Tewari, and A. Hemal, J. Urol. **174**, 2291 (2005).
[5] U. Michl, P. Tennstedt, L. Feldmeier, P. Mandel, S. J. Oh, S. Ahyai, L. Budäus, F. K. Chun, A. Haese, H. Heinzer, G. Salomon, T. Schlomm, T. Steuber, H. Huland, M. Graefen, and D. Tilki, Eur. Urol. **69**, 584 (2016).
[6] A. F. Durrani and G. M. Preminger, Comput. Biol. Med. **25**, 237 (1995).
[7] T. Minamikawa, Y. Harada, N. Koizumi, K. Okihara, K. Kamoi, A. Yanagisawa, and T. Takamatsu, Histochem. Cell Biol. **139**, 181 (2013).
[8] T. Minamikawa, Y. Harada, and T. Takamatsu, Sci. Rep. **5**, 017165 (2015).
[9] Y. Kumamoto, Y. Harada, H. Tanaka, and T. Takamatsu, Sci. Rep. **7**, 845 (2017).
[10] A. Zumbusch, G. R. Holtom, and X. S. Xie, Phys. Rev. Lett. **82**, 4142 (1999).
[11] M. Hashimoto, T. Araki, and S. Kawata, Opt. Lett. **25**, 1768 (2000).
[12] C. L. Evans, E. O. Potma, M. Puoris'haag, D. Côté, C. P. Lin, and X. S. Xie, Proc. Natl. Acad. Sci. U. S. A. **102**, 016807 (2005).
[13] H. Cahydi, J. Iwatsuka, T. Minamikawa, H. Niioka, T. Araki, and M. Hashimoto, J. Biomed. Opt. **18**, 096009 (2013).
[14] B. G. Saar, C. W. Freudiger, J. Reichman, C. M. Stanley, G. R. Holtom, and X. S. Xie, Science **330**, 1368 (2010).
[15] Y. Ozeki, W. Umemura, Y. Otsuka, S. Satoh, H. Hashimoto, K. Sumimura, N. Nishizawa, K. Fukui, and K. Itoh, Nat. Photonics **6**, 845 (2012).

[16] H. Wang, Y. Fu, P. Zickmund, R. Shi, and J.-X. Cheng, Biophys. J. **89**, 581 (2005).
[17] T. B. Huff and J.-X. Cheng, J Microsc. **225**, 175 (2007).
[18] Y. Fu, T. B. Huff, H.-W. Wang, H. Wang, and J.-X. Cheng, Opt. Express **16**, 019396 (2008).
[19] F. Tian, W. Yang, D. A. Mordes, J.-Y. Wang, J. S. Salameh, J. Mok, J. Chew, A. Sharma, E. Leno-Duran, S. Suzuki-Uematsu, N. Suzuki, S. S. Han, F.-K. Lu, M. Ji, R. Zhang, Y. Liu, J. Strominger, N. A. Shneider, L. Petrucelli, X. S. Xie, and K. Eggan, Nature Commun. **7**, 013283 (2016).
[20] M. Ji, D. A. Orringer, C. W. Freudiger, S. Ramkissoon, X. Liu, D. Lau, A. J. Golby, I. Norton, M. Hayashi, N. Y. R. Agar, G. S. Young, C. Spino, S. Santagata, S. Camelo-Piragua, K. L. Ligon, O. Sagher, and X. S. Xie, Sci. Transl. Med. **5**, 201ra119 (2013).
[21] F.-K. Lu, D. Calligaris, O. I. Olubiyi, I. Norton, W. Yang, S. Santagata, X. S. Xie, A. J. Golby, and N. Y. Agar, Cancer Res. **76**, 3451 (2016).
[22] K. Hirose, T. Aoki, T. Furukawa, S. Fukushima, H. Niioka, S. Deguchi, and M. Hashimoto, Biomed. Opt. Express **9**, 387 (2018).
[23] T. Minamikawa, N. Tanimoto, M. Hashimoto, T. Araki, M. Kobayashi, K. Fujita, and S. Kawata, Appl. Phys. Lett. **89**, 191101 (2006).
[24] J. K. Ranka, A. L. Gaeta, A. Baltuska, M. S. Pshenichnikov, and D. A. Wiersma, Opt. Lett. **22**, 1344 (1997).